Study of MDT calibration constants using H8 testbeam data of year 2004

T. Baroncelli, R.M. Bianchi, S. Di Luise, A. Passeri,
F. Petrucci , L. Spogli

Dipartimento di Fisica, Università Roma Tre
and INFN Sezione di Roma TRE, Rome, Italy

Abstract

Two sectors of the barrel and endcap regions of the ATLAS Muon Spectrometer were exposed to the CERN H8 beam in 2004. A large amount of data was collected in well controlled operating conditions. This allowed for careful study of the MDT drift properties. A better understanding of the calibration constants, of their definition and determination, and of the criteria for acceptance of the data have been obtained. Systematic effects and time stability of the constants have also been studied. Data have been found to compare well with GARFIELD predictions.

ATL-MUON-PUB-2007-004
03 September 2007

1 Introduction

In 2004 ATLAS had a long period of test beam data taking at the H8 beam at CERN. The exposed setup represented about 1 % of the experiment including two sectors of the Muon Spectrometer [1], modules of the hadronic TILE calorimeter [2] and of the electromagnetic Liquid Argon calorimeter [3]. Large samples of events were collected under different operating conditions and setup arrangements, taking data either independently with the various subdetectors (non combined runs) or using the same trigger and data acquisition system DAQ (combined runs). In the present paper an analysis of the calibration of the muon MDT chambers during that data taking period is presented, focusing on the procedure to obtain reliable calibration constants and on the study of their stability during data taking.
This paper is organized as follows: in section 2 the experimental setup of the muon stand at the H8 beam line at CERN is described; a general description of the procedure for data processing is given in section 3; in section 4 the method for the measurement of the drift time parameters is discussed; the required accuracy of calibration constants is discussed in section 5. Finally the analysis

of the test beam data is discussed in details in section 6. Details on studies using simulated data samples and on settings of GARFIELD parameters can be found in appendices A and B respectively.

2 Experimental setup

The H8 Muon stand was made of a barrel sector and an end-cap sector each one reproducing a barrel and an end-cap ATLAS sector fully instrumented with Front End electronics (FE) and equipped with the alignment system.
Both precision tracking chambers (MDT and CSC) and trigger chambers (RPC and TGC) were installed. The trigger was provided by external scintillation counters as described in the following.
The barrel setup consists of six MDT chambers (two chambers for each type: inner BIL, middle BML and outer BOL stations). There were also six RPC doublets; two were placed next to each BML and one next to each BOL station. In the end-cap stand there are 6 MDT chambers: two inner (EI), two middle (EM) and two outer (EO) and three TGC units (one triplet and two doublets). Two additional barrel stations were used in the test stand: one BOS station (MDT and RPC) upstream of the muon wall for Combined Test Beam (CTB) studies and one MDT chamber of type BIL placed on a rotating support remotely operated and controlled (called $BILrot$ in the following). The support allowed rotations of up to ± 15 degrees around the axis of the chamber to enlarge the angular range of muon tracks for the calculation of the space time relation ($r-t$ in the following) of the corresponding run. One CSC chamber was also installed and integrated in the combined data taking. Finally, one magnet was positioned between the $BILrot$ and the BIL chambers and was used to swap the beam spot. The magnet current was controlled remotely and varied from 0 A up to ± 600 A, providing a maximum field integral of about 4 Tm. The layout of the experimental area is shown in Fig. 1.

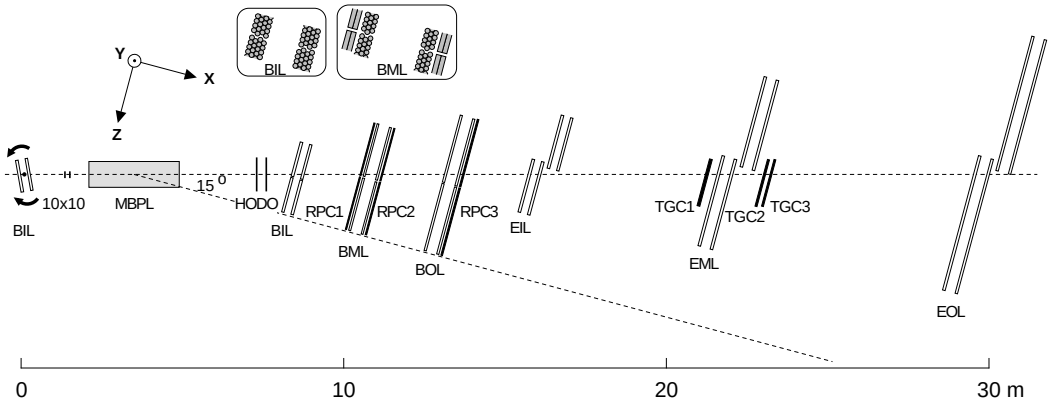

Fig. 1. Schematic view of the 2004 muon setup in the H8 area

The trigger was provided by two different types of scintillators: a coincidence between two small scintillators covering a surface of about *10×10* cm^2 (called *10×10* trigger) that selected the core of the H8 muon beam and a coincidence between two planes of large scintillators covering a surface of about 60×100 cm^2 and the veto of the *10×10* (called *hodoscope* trigger) that selected muons in the beam halo for a large coverage of the muon setup. In this second case beam muons cross the tubes at different distances from the readout electronic side (RO) and the signal propagation time along the wire has to be taken into account. As the *10×10* trigger selects muons passing at a constant distance, only data taken in this condition were used and no offline correction was applied in this analysis.

The signal from each tube is amplified, shaped and discriminated by the ASD chip [4] and the processed signal is sent to the AMT [5] TDC chip which measures the threshold crossing time. Also the amount of charge collected in a programmable time interval after the threshold crossing is measured via a Wilkinson ADC. Three octal ASD chip and one AMT chip are contained in a mezzanine front-end board which serves 24 tubes. The CSM (Chamber Ser-

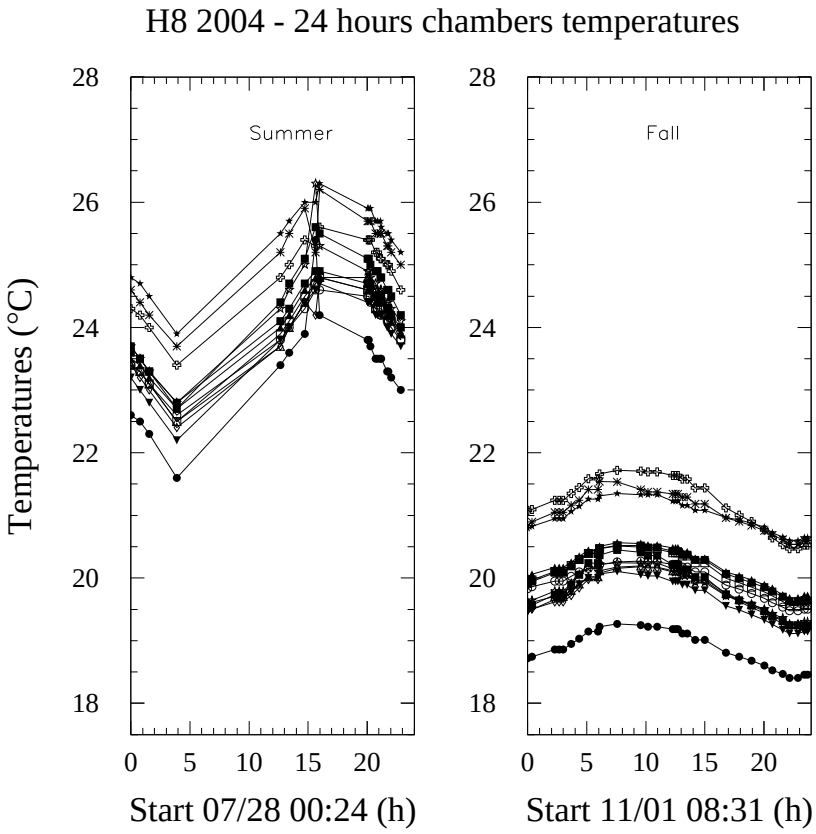

Fig. 2. Mean temperature as recorded in the different chambers as a function of time for a time interval of 24 hours in summer (left) and fall (right).

vice Module, [6]) is an on-chamber board which distributes the main 40 MHz clock, collects the data from the mezzanines of one chamber and sends them via optical fibers to two prototypes of the Muon Read Out Driver (MROD) which are VME boards controlled by the ATLAS DAQ-1 system. An additional mezzanine board was used to encode the time of the trigger signal since this was asynchronous with respect to the CSM clock.

The monitoring of the parameters of the spectrometer working conditions are controlled via the Detector Control System (DCS) [7]. This includes the settings of the programmable parameters of the front-end electronics (for example the discriminator thresholds which were varied between 34 and 52 mV in different runs) and the monitoring of the environmental parameters. In particular the temperature of each chamber was measured at different locations on the chamber by means of temperature probes at regular time intervals. The measurements were stored in the Condition Data base. As an example, the mean temperature recorded on all chambers in a 24 hours time interval in summer and fall is shown in Fig. 2; a night/day variation is clearly visible.
Data samples in different operating conditions were taken with the muon system only during the summer (Summer data) or simultaneously with the Tile and LAr calorimeters in fall (Fall data); they are listed in table 1. The samples used in the present analysis were taken in a few days during these two

period	**threshold**	**# runs**	**total events**
Runs in summer	34	18	440 k
	36	56	1349.6 k
	40	89	4992 k
	44	67	2490 k
	48	4	120 k
	52	5	126 k
Runs in fall	38	1	370 k
	40	80	6106 k
	42	1	240 k
	44	1	306 k
	46	1	204 k
	48	1	151 k
	50	1	150 k
	52	2	300 k

Table 1
Data samples used in the analysis.

periods. The momentum of beam particles of the samples used in the present analysis was larger than 100 GeV/c, ranging between 100 and 250 GeV/c in the summer and between 180 and 250 GeV/c in fall.

Information on the horizontal profile of the beam can be obtained by the MDT hit occupancy plot in the different chambers. In runs taken with the *10×10* trigger the beam spot illuminates 2-3 tubes, which corresponds to a range of 6-9 cm. The occupancy plot of each run has been parametrized as the superposition of two Gaussian distributions. This fit procedure has been repeated for all chambers in all runs taken with the *10×10* trigger. Out of the two Gaussian distributions used to parametrize the beam profile one is narrow (less than 2 tubes wide) with a large peak value and has been taken to represent the core of the beam spot while the other is wider (about 10 tubes). The shape of the beam profile was stable within approximately one tube between summer and fall. The peak position of the beam spot as a function of the day in 2004, as measured in the EOS chamber, is shown in Fig. 3. The left and the right part of the figure refer to the summer and fall

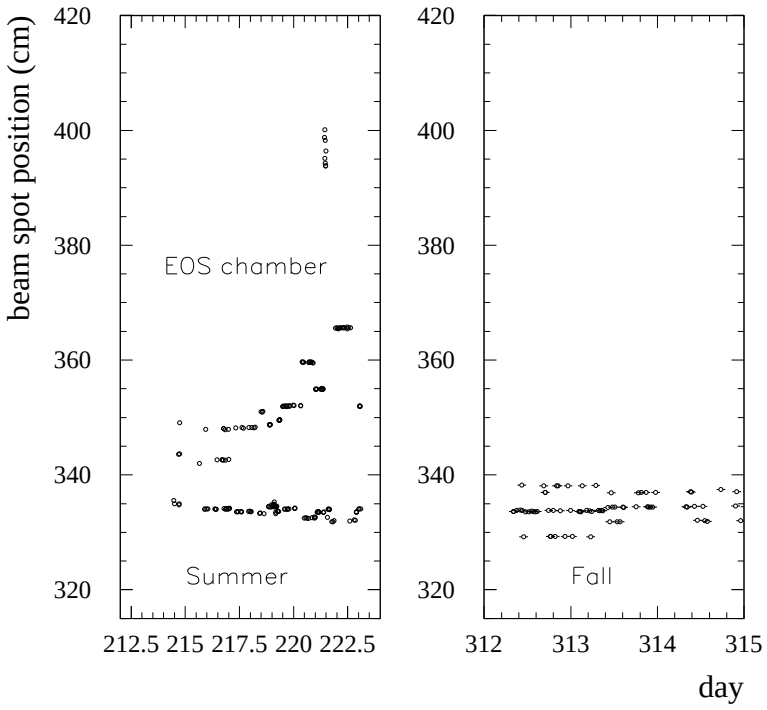

Fig. 3. Beam spot position as measured in EOS chamber as a function of the day number in year 2004. The two bands in the left diagram correspond to measurements with and without magnetic field.

periods of data taking respectively. Both data taking periods are characterized

by the presence of one main band accompanied by one or more bands due to different magnet currents. The position of the central band, corresponding to the magnet being off, is observed to be stable between summer and fall.

3 Offline data analysis

A sequence of calibration steps has to be performed to reconstruct tracks from raw MDT data (i.e. tube identifiers and TDC information). The first step is the determination of the t_0 for each tube defined as the drift time associated to a particle crossing the tube at a distance r=0 from the wire representing a relative delay between different channels. This value has to be subtracted from the time measurements. As will be discussed in the next sections, the t_0 is computed using a fit procedure to the drift time distributions which returns also other parameters of the drift time distribution as the maximum drift time t_1. This first calibration step does not require any track reconstruction. Once the normalized drift time has been computed, it is converted into a drift radius using the $r - t$ relation.
The track reconstruction is a two step procedure: first, hits that can be associated to form a track are selected (pattern recognition); then a fit with a line tangent to the drift circles (circles centered on the wire with radius equal to the drift radius) is performed. The determination of the $r - t$ relation requires a dedicated iterative procedure (autocalibration, see [8]) which is based on the reconstruction of large samples of muons.
All the analysis presented in this work was performed using the Calib program [9]. Calib is a package (developed in Roma Tre and Roma "La Sapienza") for the analysis of MDT data, in particular for the autocalibration of the chambers and for the evaluation of resolution and efficiency.
The GARFIELD Monte Carlo program represents the most accurate simulation of the physics processes and of the electronics which characterize the behaviour of a drift detector and has been used for comparison with data. Actually it is made up of three packages: HEED[10], MAGBOLTZ[11] and GARFIELD[12] itself. The HEED program computes the energy loss of fast charged particles in gases, taking delta electrons and multiple scattering into account. The program can also simulate absorption of photons in the gas via a photo-ionization mechanism. The MAGBOLTZ program, computes electron transport parameters, for example, mobility Townsend and the diffusion coefficients, for a large variety of gases and gas mixtures. The program is based on the numerical solution of the Boltzmann transport equation. The principal initialization parameters are: gas composition, temperature, pressure and electric (magnetic) field range. GARFIELD is a program for the simulation of two and three dimensional drift chambers. It is interfaced to HEED and MAGBOLTZ and computes field maps, electron and ion drift paths, drift time

maps and arrival time distributions, signals induced on the wires by drifting electrons and ions as well as the electronics response via a user defined transfer function. Details on the used setting of different GARFIELD parameters are given in appendix B.

4 Determination of drift time spectra parameters

All drift time distributions studied in this paper were fitted with one or more Fermi Dirac functions. The performance of several fit functions has been studied and the relative merits will be presented in this section.
The first fit function considered in the present analysis, called Classic t_0 in the following, consists of two distinct Fermi Dirac functions describing the leading and trailing edge with an exponential function for the central part. The analytic expression of the function is given below:

$$f(t) = p_1 + \frac{p_2 \left(1 + p_3 e^{-\frac{t-p_5}{p_4}}\right)}{\left(1 + e^{\frac{-t+p_5}{p_7}}\right)\left(1 + e^{\frac{t-p_6}{p_8}}\right)} \tag{1}$$

The parameter p_1 is the uncorrelated (flat) background, p_2, p_3 and p_4 describe the shape of the central part of the distribution, p_5 is the t_0 of that given tube, p_6 is the maximum drift time, p_7 and p_8 describe the leading and trailing edges (*slope* and $slope_{te}$ respectively in the following). The fit is done in three steps; first with 6 parameters (fixing p_7 and p_8 to initialization values) then p_7 is set free and at last the fit with 8 free parameters is performed.
As an example, a typical drift-time distribution and the corresponding fit is shown in Fig. 4.
For some applications, only a fit to the first part of the drift distribution may be sufficient to compute the t_0 value. The corresponding function, called Fermi Dirac t_0 in the following, is defined as:

$$f(t) = \frac{p_1}{\left(1 + e^{-\frac{t-t_0}{p_3}}\right)} \tag{2}$$

In the expression above p_3 describes the width of the leading edge.
It is important to notice that the t_0 value defined in both functions and determined by a fit procedure to the drift time distribution does not correspond to the start of the physical drift time window but is close to the half height position of the leading edge. It is thus significantly shifted to later times with respect to the start of the physical drift time window. However, as the drift times, determined for each tube, are related to this value, the systematic shift will be all reabsorbed in the definition of the $r - t$ relation. The importance

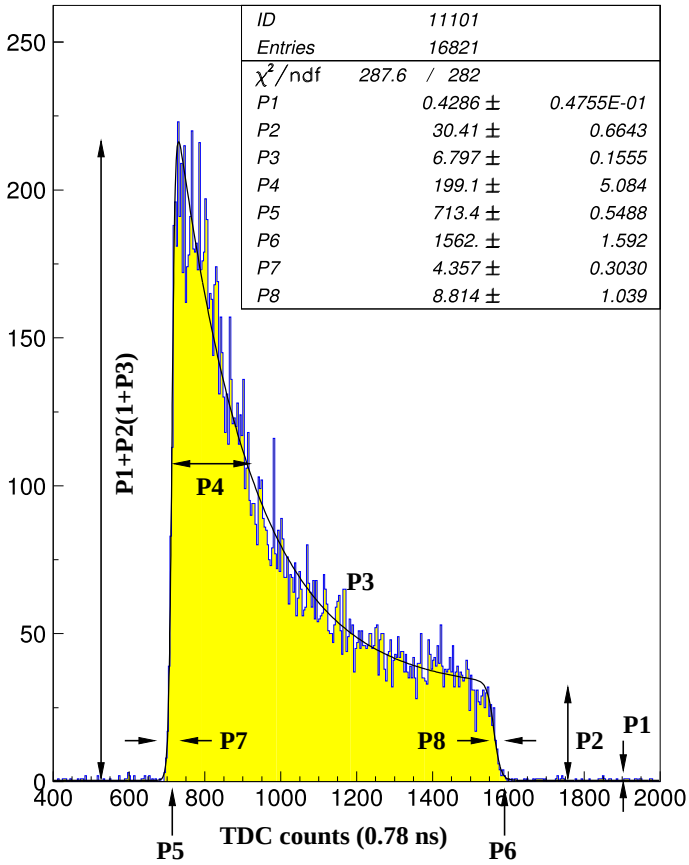

Fig. 4. Typical drift time distribution at nominal operating conditions. The fitted Classic t_0 function described in the text is also shown.

of the t_0 determination is in the fact that the starting points of the time distribution for all MDT tubes should be equalized.
A detailed study of the optimal determination of the t_0 parameter has been performed and is described in appendix A. The main result of the analysis presented there is that the best estimator for the starting point of the MDT drift distribution is a linear combination of t_0 and of the p_7 parameter describing the leading edge slope. The new parameter, called "Displaced Classic t_0", being defined as $t_0 - 1.5 \times slope$ is used in the rest of the paper. The Displaced t_0 algorithm gives a width of 0.75 TDC counts for samples of 5k events and 0.25 TDC counts for samples of 50k events. A study of the drift spectrum length t_{max}, defined as $p_6 - p_5$, is also reported in appendix A. Similarly, Displaced t_{max}, being defined as $t_{max} + 1.2 \times slope_{te}$, is introduced and shown to give the optimal determination of the drift spectrum width.

5 Required accuracy of MDT calibration constants

The ATLAS muon spectrometer is designed to reconstruct muons with energies up to several TeV's. The target muon momentum resolution of 10% at 1 TeV imposed requirements on the alignment system, as well as on the calibration constants of MDT chambers. Initial studies on the contributions of different effects to the momentum resolution in the muon spectrometer are presented in [1], showing that the contributions of tube resolution and autocalibration dominate the momentum resolution for transverse momenta p_T above 300 GeV, both in the barrel and in the endcap regions. The impact of miscalibration has been further studied in [13] using large samples of simulated single muons generated according to a flat distribution in η and ϕ. Generated tracks are reconstructed using standard muon reconstruction packages and combined with tracks in the inner detector.
The width of the $p_{T,reco}^{-1}/p_{T,truth}^{-1}$ distribution has been used to estimate the momentum resolution, where $p_{T,reco}^{-1}$ and $p_{T,truth}^{-1}$ are the inverse transverse momenta of the reconstructed and of the simulated muon respectively. The impact of small offsets in the calibration constants on the reconstruction of simulated tracks, generated using perfectly calibrated chambers, was studied. In particular the effect of mis-calibration in t_0 and in $r-t$ has been analyzed. The impact of miscalibrated t_0 has been studied both by adding a fixed offset t_{shift} to all t_0's ($t_0^{mis} = t_0 + t_{shift}$) or by adding a Gaussian distributed random shift $G(\sigma_{spread})$ to each individual t_0 ($t_0^{mis} = t_0 + G(\sigma_{spread})$). In the first case a shift smaller than 2 ns is needed to achieve an overall resolution of 8 % at 1 TeV (not including alignment effects). A shift of 5 ns would cause a worsening of the momentum resolution to 12 %. The momentum resolution is less affected in the case of a Gaussian distributed random t_0 shift, due to the fact that the net effect is zero by construction.
The miscalibration of the $r-t$ relation has been parametrized with a parabolic deformation which leaves the geometrically fixed start and end point of the $r-t$ relation untouched. The $r-t$ deformation has a maximum of Δr_{max} at half the tube radius. The effect of $r-t$ miscalibration has been studied for different values of Δr_{max} and different values of the initial muon momentum. The impact of the $r-t$ miscalibration on the muon momentum resolution is observed to be non linear and most significant at high momenta. A shift of 100 μm induces a deterioration of 5 % for transverse momenta larger than 50 GeV. To achieve an overall contribution of 8 % due to single tube resolution and miscalibration the maximum deformation of the $r-t$ relation should be smaller than 50 μm. Thus 2 ns and 50 μm are the target accuracies for the t_0 and $r-t$ determination respectively.

6 Study of MDT calibration constants using H8 test beam data

This part of the paper describes the results obtained using data samples taken at H8 in 2004. Subsection 6.1 describes the way tubes are selected for the analysis; subsection 6.2 contains an analysis of the time stability and systematics of the time constants while subsection 6.3 refers to the study of space time relation determination and relative systematics.

6.1 Quality Acceptance of MDT calibration constants

Fit parameters of drift distributions of MDT tubes have been used to find abnormal values of fit parameters. The distributions of the following fit parameters have been studied to determine validity intervals for the parameters to be acceptable:

- the noise level of the tube, strictly related to the p_1 parameter,
- the leading edge slope (p_7),

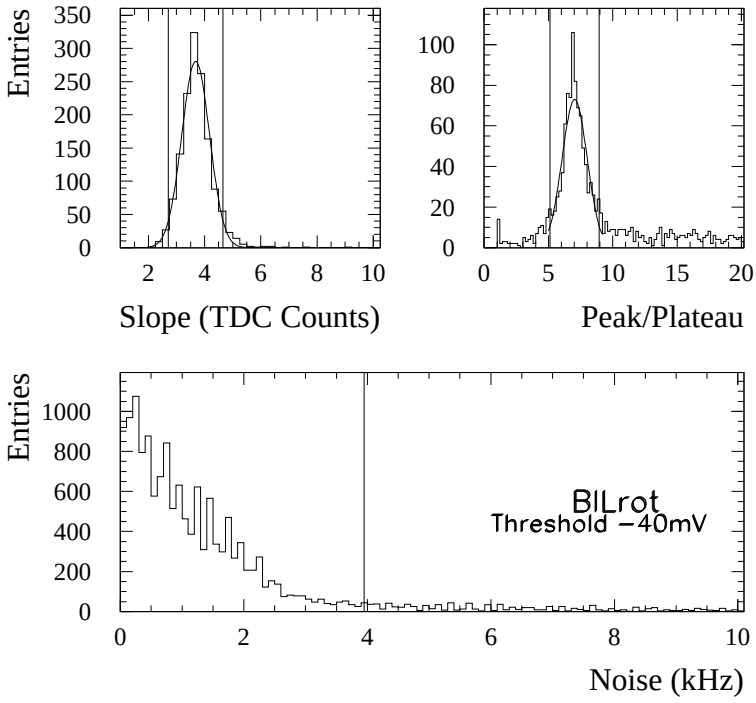

Fig. 5. Distribution of the quantities used for tubes selection: slope(top left), ratio peak/plateau (top right) and noise (bottom). Vertical lines indicates distribution cuts.

- the drift spectrum length ($p_6 - p_5$),
- the ratio between the peak of the distribution and the plateau, defined as $\frac{p_1+p_2(1+p_3)}{p_2}$ (see Fig. 4).

The leading edge slope, the drift spectrum length and the peak over plateau ratio have been described by Gaussian distributions with non Gaussian tails, while the noise level has a falling shape with a long tail. The interval of validity of parameters with Gaussian distribution was chosen as $average \pm 1.96 \times \sigma$ of the fit function. A single cut on tube noise distribution was chosen as to leave 5% of the distribution out. If a tube does not satisfy all selection cuts, it will not be included in the analysis. Numerical values of the cuts depend on chamber type and threshold. A distribution of some parameters is shown in Fig. 5 for the $BILrot$ chamber, at a 40 mV threshold as measured during the summer period data taking.
In some cases the MDT drift distributions of some chambers have been observed to undergo time shifts. Only stable periods are considered in the present paper.

6.2 Study of t_0

6.2.1 t_0 stability with time.

The time stability of MDT drift properties has been studied with two different methods: the time stability of single tubes of all chambers and the time stability of the average of all tubes of one multilayer. The stability in time of the position of the beam spot has the consequence that the most illuminated tube of each layer is always the same and that the multilayer average has a composition that is constant in time. Due to the small size of the H8 beam spot, the number of MDT tubes with sufficient statistics to compute MDT calibration constants is less than two or three tubes per layer. Thus, a systematic comparison on the response of close-by tubes is very difficult.
The most illuminated tube of each layer and chamber was selected from the tube occupancy map and used to derive the first results presented below. The three barrel chambers and three endcap chambers give a total of 40 layers; these 40 tubes in total, one per layer, were studied as a function of time.
The t_0 trace plot of one BIL tube is shown with respect to the day in 2004 in Fig. 6 for summer and fall period. The left part of the trace plot is clearly more scattered than the right part. The same pattern is observed in all trace plots of all tubes and may be explained by a significant difference in the average length of summer runs with respect to fall runs. In fact the runs taken during the last period of the year are, in average, four to five times longer than in summer. Fig.7 shows the distribution of the number of entries of all the tubes in all the runs used in the analysis of t_0 stability at a threshold of 40 mV.

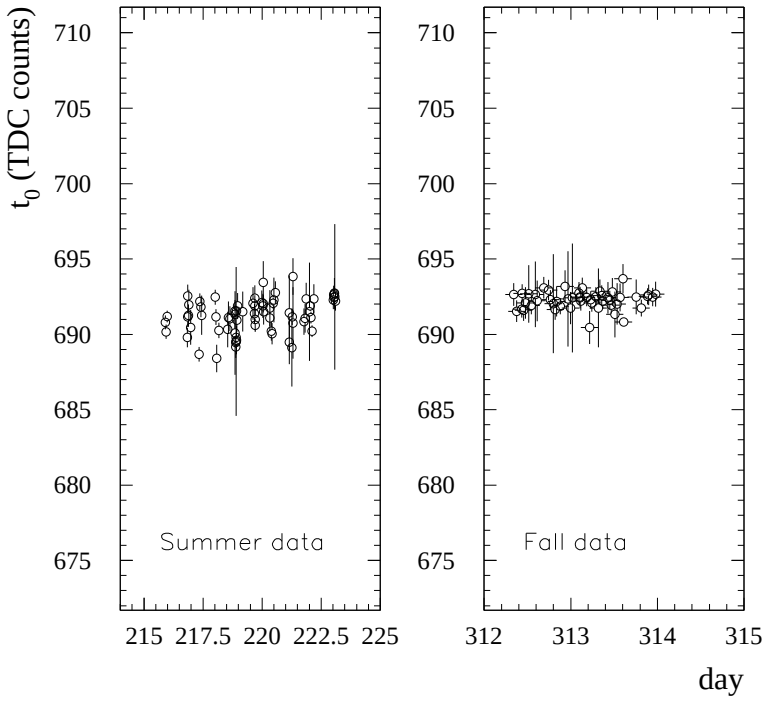

Fig. 6. t_0 trace of most populated tube of BIL chamber

Left part of the figure refers to fall, the right part to summer. Indeed the most probable value is observed to be around 20k and 6k for fall and summer data respectively. The average value changes by about a factor of two.
To quantify the stability of the measured t_0 values, all single tubes considered in this analysis have been separately studied. The t_0 distribution of each tube and separately for the summer and for the fall, has been fitted with a Gaussian distribution. The fitted width has been taken to be a good indication of the stability of tubes.

The results of this study are shown Fig.8 for the 40 mV threshold sample. The top and bottom part of each figure shows the fall and summer data taking periods, respectively. The widths of t_0 in the fall data taking period is seen to cluster around a value of about 0.5 TDC counts corresponding to less than 0.4 ns dispersion for both the barrel and the endcap. The largest t_0 spread during this period is observed to be of the order of 0.8 TDC counts in the barrel and 1.3 TDC counts in the EOS chamber of the endcap. The spread of t_0 observed during the summer data taking period is larger than in the fall by a factor of about 2 and is again fully understood as being due to difference in length of runs taken in the different data taking periods. In particular the t_0 average spread observed in the summer and in the fall agrees well with the calculation shown in Fig. A.6 for an average run length of 10k and 5k events for the fall

and summer respectively.
The spread of the Displaced t_0, defined as

$$\text{Displaced Classic } t_0 = \text{Classic } t_0 \text{ - } \textit{correction factor} \times \textit{slope}$$

as a function of the correction factor itself, has been studied in Appendix A and shown to be minimal for a value of 1.5. One of the most illuminated tubes of the BIL2 chamber has been used to investigate how the spread of the t_0 is observed to change in data as a function of the correction factor introduced in Appendix A. The result is shown in Fig.9. Triangles correspond to data, open circles and squares correspond to simulated data with a sample size of 5000 events and 10000 events respectively. The distribution of the number of entries of the most illuminated tube collected in each of the runs used in this analysis is shown in the insert. The distribution is observed to start at 5000 entries, has a peak at about 20000 events and an average value of $13.8K$events. The low multiplicity tail of the distribution is likely to bias the spread of the t_0 distribution.
The average value of the Gaussian fit describing the distribution of drift times of one MDT tube has been assumed to be representative of the average t_0

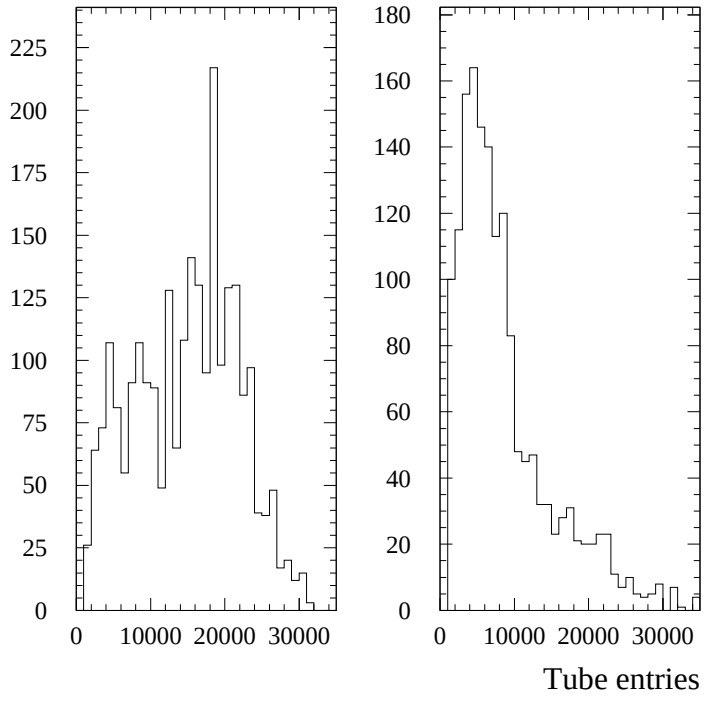

Fig. 7. Distribution of the number of entries of most populated tubes used in the present analysis,left part corresponds to summer, right part corresponds to fall

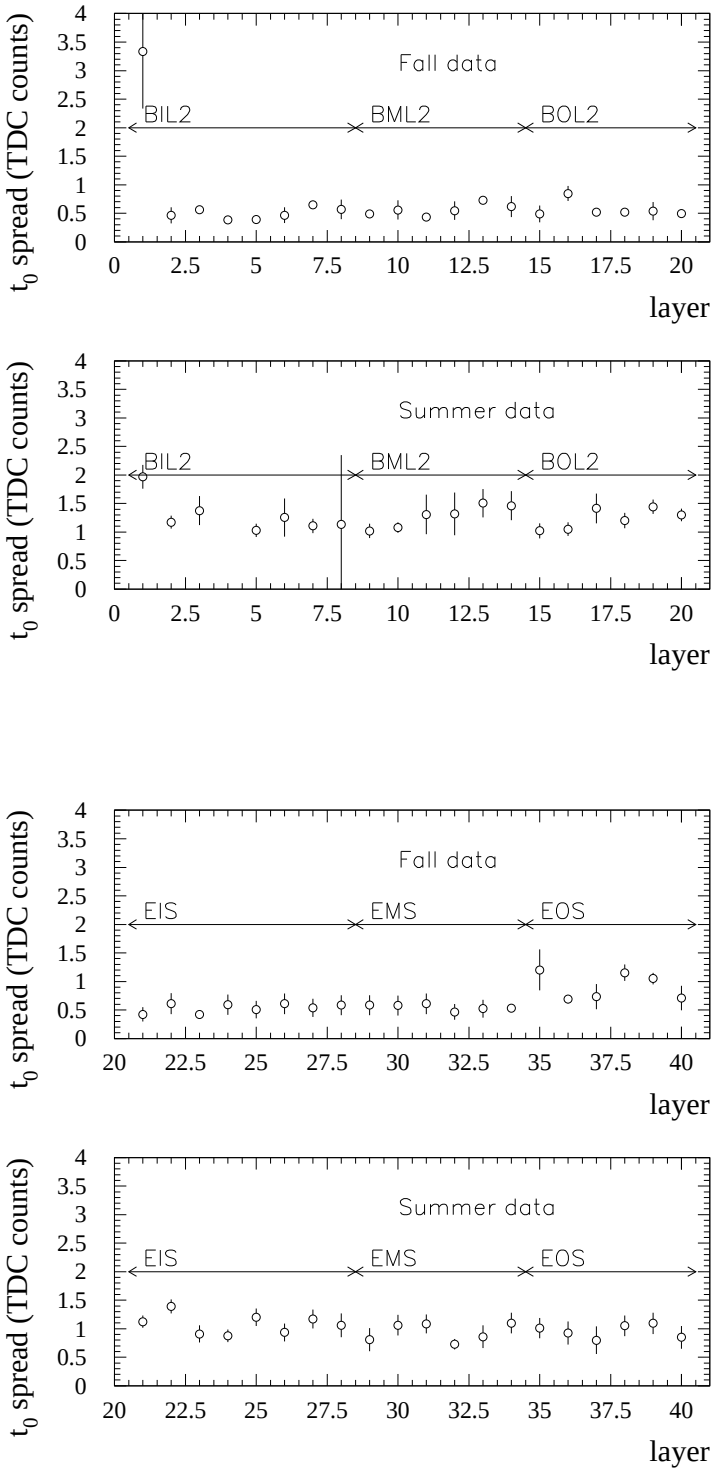

Fig. 8. Width of the t_0 distribution for different layers of the chambers as measured at 40 mV threshold

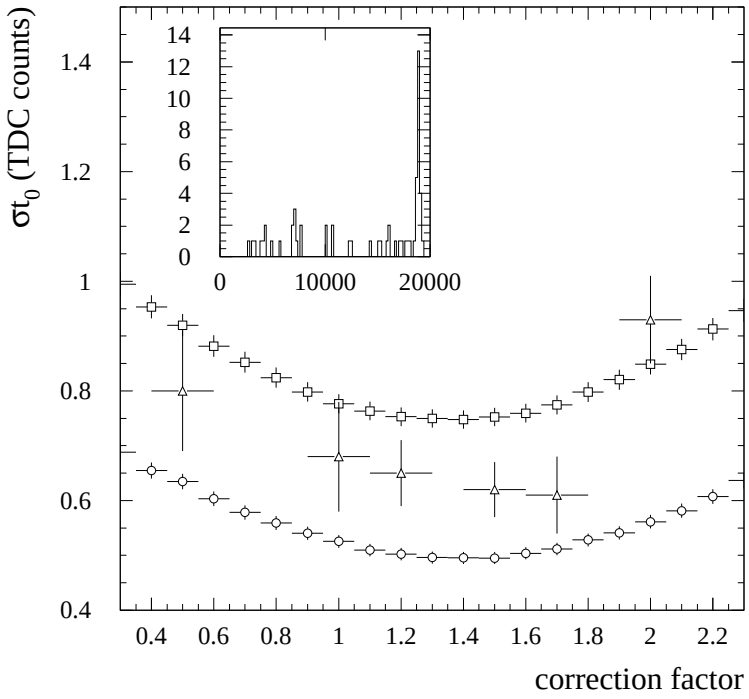

Fig. 9. Spread of the Displaced t_0, defined as Classic t_0 - $correction factor$ $\times$ slope, observed in data as a function of the sample size; triangles correspond to data, open circles and squares correspond to simulated data with a sample size of 5000 events and 10000 events respectively. The distribution of entries of tubes used in this analysis is shown in the insert. This spread has been studied in Appendix A and shown to be minimal, in simulated events, for a value of 1.5 of the slope.

value. The distribution of the difference of the average t_0 value between fall and summer is shown in Fig. 10. The distribution has been fitted with a Gaussian distribution with an average value of 0.85 TDC counts and a spread of 0.30 TDC counts. This effect has also been studied using GARFIELD. The predicted difference for a temperature gradient of 5^oC was found to be 0.6 ± 0.1 TDC counts, in qualitative agreement with experimental findings. A variation of about 5°C between summer and fall induces an increase of the drift spectrum length (p_6 - p_5) which may result in a change of the correlation between p_5 and p_7. As a counter-proof no significant shift in the t_0 is observed (both in the data and in the simulation) once only the first part of the distribution is fitted using the function of eq. 2.

A time stability analysis, similar to the one described above for single most populated tubes, has been performed on the multilayer average t_0 of all MDT chambers. First, all tubes of the same multilayer are selected using the procedure described in section 6.1. The t_0 distribution of the selected tubes of one

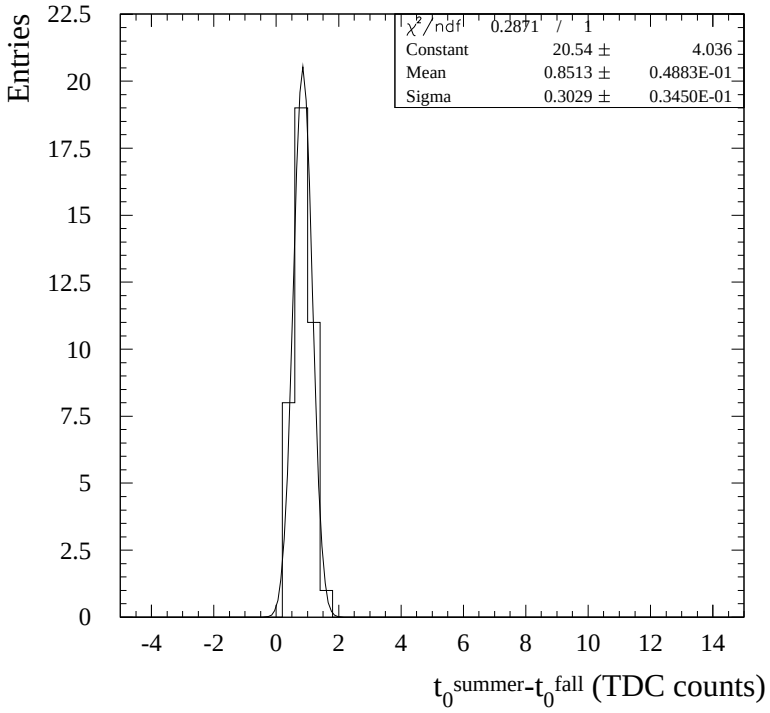

Fig. 10. Distribution of mean t_0 variation for all the tubes between fall and summer

run is then fitted with a Gaussian distribution assumed to be representative of the multilayer average t_0 and of the multilayer t_0 spread. The trace plot of the multilayer 1 average t_0 of the BIL chamber is shown in the top part of Fig.11 as a function of the run number and as measured at a threshold value of 40 mV. Summer and fall periods are both included in the plot. The distribution of t_0-$<t_0>$ is shown in the bottom left and right part of Fig. 11 for summer and fall runs respectively. A Gaussian fit is also shown. The width of both distributions is less than 0.8 TDC counts.

The procedure described above has been repeated for all multilayers of 6 MDT chambers and for thresholds of 36, 40 and 44 mV. This corresponds to 2 multilayers $\times$ 6 chambers $\times$ 3 thresholds = 36 entries and is summarized in Fig.12 where the width of distribution of the multilayer average t_0 for different chambers and different thresholds is shown. For each chamber (indicated in the figure with an horizontal arrow) 6 points are given. The first three points refer to the first multilayer while the second group of three points refer to the second multilayer. Each sequence of three points corresponds to the spread of the difference t_0 - average t_0 at the thresholds of 36, 40 and 44 mV, respectively. All points cluster around 1 TDC count. Within statistical errors the 36 mV point is, as expected, the one with smaller spread. This indicates a good time stability of multilayer average t_0.

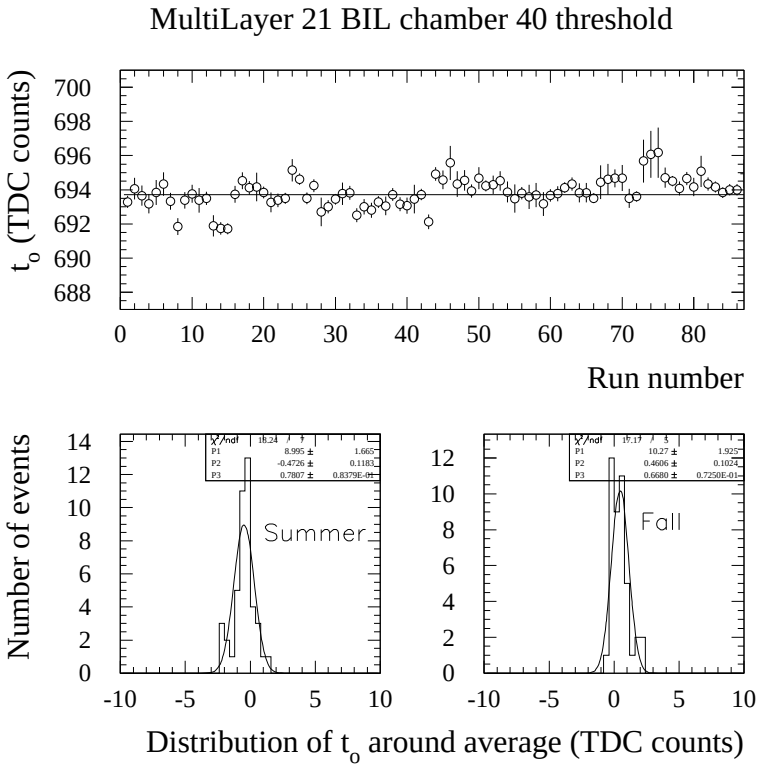

Fig. 11. Trace plot and distribution of multilayer average t_0 for BIL chamber at 40 mV threshold

6.2.2 t_0 systematics: threshold and position.

The MDT readout electronics is characterized by an adjustable discriminator threshold value which affects the value of t_0. Data taken at different thresholds have been used to study the variation of t_0 at different electronics thresholds. Since most data were taken at a threshold value of 40 mV, chosen as the standard working point of MDT chambers, the difference $t_0^{threshold}$-t_0^{40mV} was chosen to quantify the variation of t_0 with threshold. This choice is justified by the fact the variation of $t_0^{threshold}$-t_0^{40mV} is expected to be the same for all chambers, while t_0 at the same threshold changes with the chamber position, thus making the comparison difficult. The same sample of well populated tubes in different chambers used in the analysis of stability of single t_0's has also been used to study $t_0^{threshold}$-t_0^{40mV}. The distribution of this variable for all the chambers and using all selected tubes has been constructed and fitted with a Gaussian distribution. The average value of the fitted function for each threshold, and its error, is taken to be representative of the change with threshold in the different chambers. In Fig. 13 t_0^{40mV}-$t_0^{threshold}$ is shown with respect to $t_0^{threshold}$ in the range between 34 and 48 mV for the rotating BIL chamber. Open star points were obtained using GARFIELD at 30, 35 and 40 mV. The agreement between data and simulation is good. As expected the slope of the

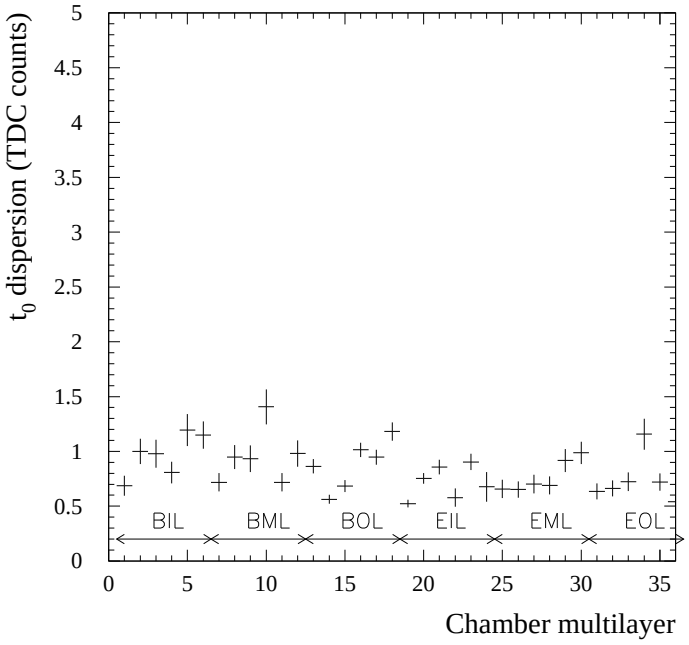

Fig. 12. Width of distribution of multilayer average t_0 for different chambers and different thresholds

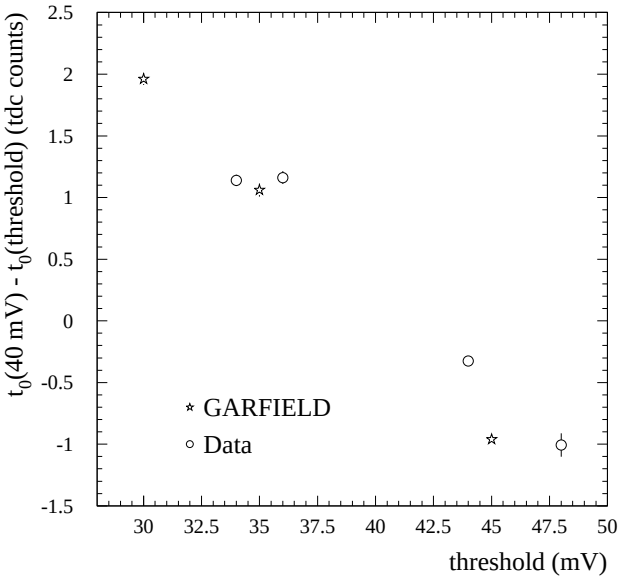

Fig. 13. Variation of t_0 as a function of threshold

variation is negative and amounts to about 0.13 ns/mV. The same quantity has also been computed using GARFIELD which gave a value of 0.15 ns/mV, in good agreement with data.

The absolute value of t_0 is expected to depend almost uniquely on the chamber position. Other effects are expected to be less important like chamber electronics and environmental conditions. The result is shown in Fig. 14 where the multilayer averaged t_0 is shown as a function of the multilayer position for the 40 mV threshold. Different thresholds have an almost identical pattern, except for minor differences in the absolute t_0 value. Experimental points, from left to right, correspond to BIL, BML, BOL, EOS, EOM, EOL chambers respectively. The observed slope corresponds to $\sim$ 24 cm/ns. This number is not identical to the velocity of the muon (=c), because the signal propagation time along the wire from the beam spot to the read-out side was not taken into account. Furthermore, the distance between the chambers is not the path travelled by the beam particles which have an angle of about 15 degrees with respect to the chamber axis. Finally the length of the optical fibers, where signals propagate at a speed of 20 cm/ns, (i.e. the phase of the clock) was assumed to be the same for all chambers.

6.2.3 t_{max} temperature systematics.

The total length of the drift time distribution, t_{max}, has also been studied and found to be best described by *Displaced* t_{max} as shown in appendix A. While t_0 is known to have very little temperature dependence, t_{max} is expected to have a significant dependence on temperature[14]. It has already been shown in Fig. 2 that there is a non negligible systematic temperature

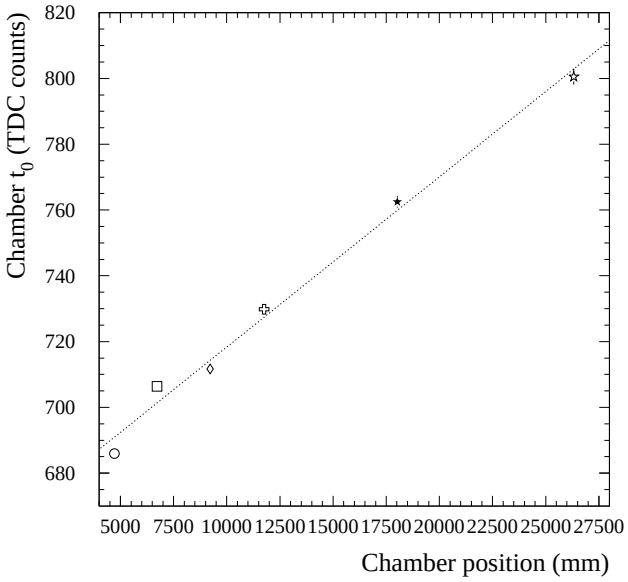

Fig. 14. Chamber t_0 as a function of the chamber position as measured at 40 mV threshold

difference among the different chambers of $H8$ experimental setup. Thus in order to compare the total length of the drift time distribution of different chambers the dependence of t_{max} on temperature of each chamber has to be studied. The multilayer average t_{max}, similarly to what was already done for the t_0, was defined as follows. First all tubes of the same multilayer are selected using the procedure described in section 6.1. The t_{max} distribution of the selected tubes of one run is then fitted with a Gaussian distribution and the fitted mean value was defined to be the multilayer average t_{max}. The corresponding temperature measurement for a given run and chamber was read from the Condition Database. The correlation plot between t_{max} and temper-

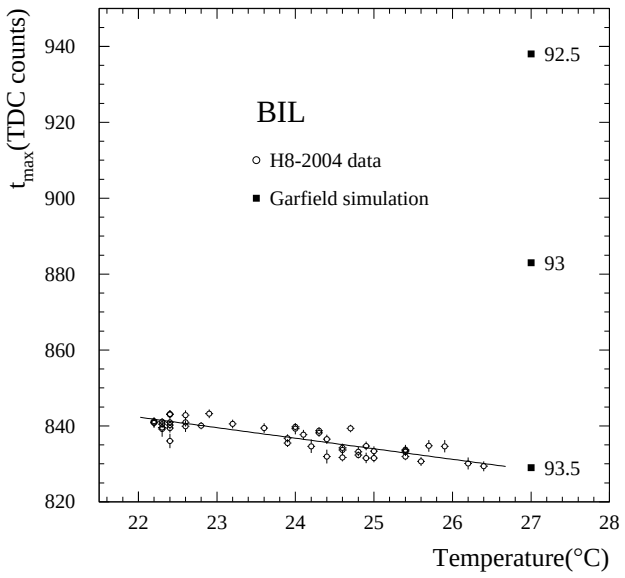

Fig. 15. Observed drift spectrum length temperature dependence for the BIL chamber. GARFIELD simulated points at 27° C and for different gas compositions are also shown.

ature is shown in Fig.15 for the BIL chamber. The GARFIELD simulation was used to compute t_{max} for a temperature of 27° C and for three different CO_2 fractions of the MDT gas. The point at the nominal gas composition is observed to disagree with data while a good agreement is observed for a gas composition of about Ar CO_2 of 93.5:6.5. It should be noted that while the gas composition is believed to be very stable in time, the absolute gas mixture, as produced by the gas system is not accurately known.
The correlation plot between t_{max} and temperature is shown in Fig.16 for different chambers. Each correlation plot was fitted with a straight line defined as $t_{max} = (\text{T-}24^\circ\ C) \cdot \text{slope} + t_{max}^{24^\circ}$. The average value of the distribution of the slope and of $t_{max}^{24^\circ}$ for the different chambers has a mean value -(2.5±0.1) ns/°C and of 673.9±0.5 ns, respectively. The spread of the two distributions is of 0.4±0.1 ns/°C and of 2.0±0.4 ns, respectively. The spread of $t_{max}^{24^\circ}$ is non neg-

ligible and may be caused by different gas properties in the different chambers.

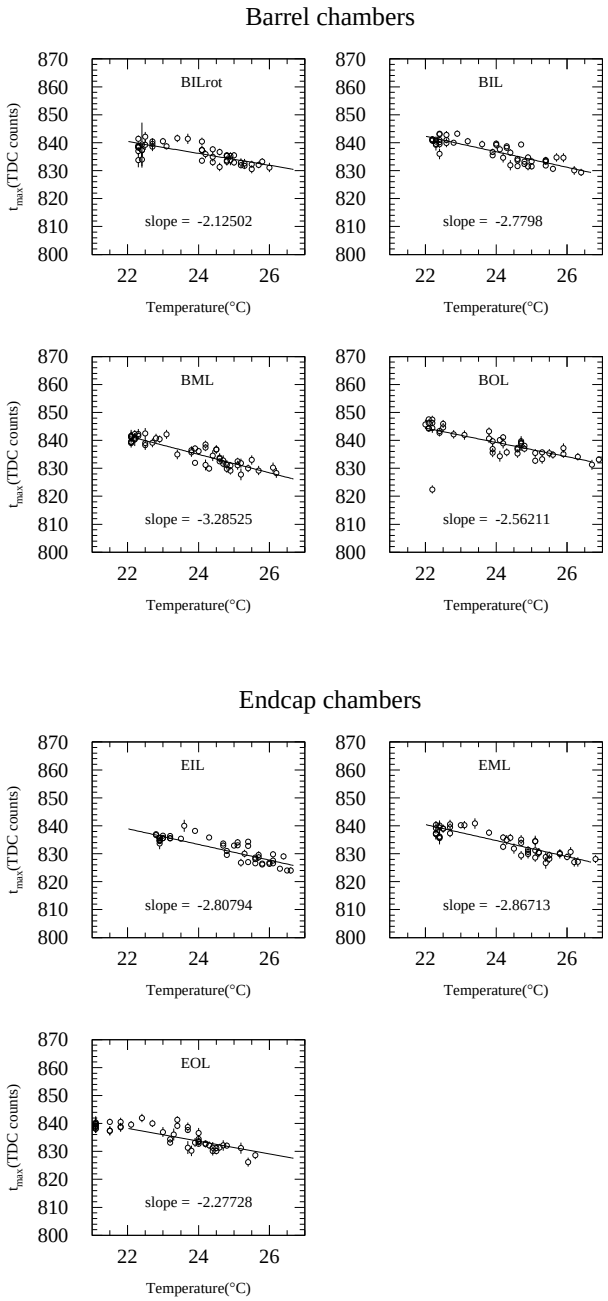

Fig. 16. Length of drift spectra versus temperature for barrel and endcap chambers.Each correlation plot was fitted with a straight line defined as t_{max} = (T-24° C) · slope + $t_{max}^{24°}$. The average value of the distribution of the slope and of $t_{max}^{24°}$ for the different chambers has a mean value -(2.5±0.1) ns/°C and of 673.9±0.5 ns respectively. The spread of the two distributions is of 0.4±0.1 ns/°C and of 2.0±0.4 ns, respectively.

6.3 Study of $r-t$ relation.

The exact shape of the nonlinear $r-t$ relation of the Ar/CO_2 gas mixture (93/7% nominal) depends on pressure, temperature and gas conposition. The gas distribution system of the H8 setup was made of a single gas mixer which supplies all chambers. Thus the gas composition (Ar/CO_2 percentage) is assumed to be identical for all chambers while a difference in gas contamination (air or water vapor) and in pressure may occur because of leaks in the gas connections. The only directly measured parameter is the temperature (Fig.2) which may change with time and position of the chambers in the hall. A mean temperature difference of the order of 5°C is observed between summer and fall, while a difference of the order of 2°C is measured between the coldest and the warmest chamber at a given time.
Fig.17 shows an example of one computed $r-t$ function for a summer run at 40 mV threshold which has been used as a reference for the temperature studies described below. The insert in the figure shows the average residuals as a function of time as obtained in the last step of the calculation when the desired convergence is reached. The mean value of the residuals is within $\pm 3\mu$m.
The effect of temperature variation on the $r-t$ has already been studied in laboratory tests [14] and was presented as difference between two $r-t$'s with a given temperature difference. The difference has been observed to vary with the drift.For a positive temperature difference it is lower than zero for small

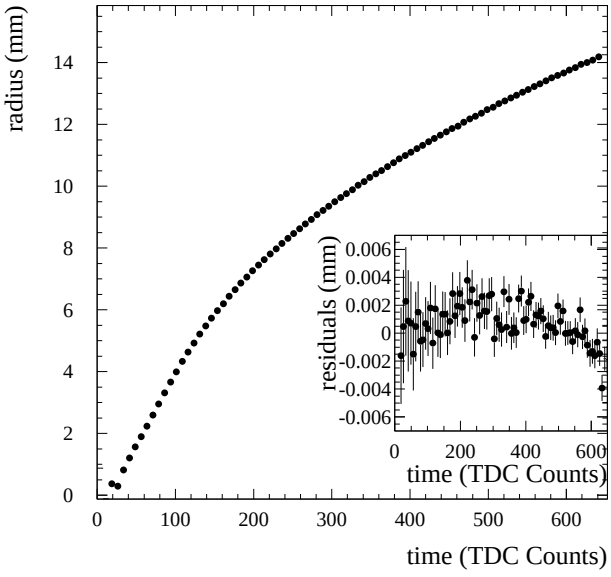

Fig. 17. Typical $r-t$ function as measured in summer using $BILrot$ data. The insert shows the residuals versus drift time.

drift times (lower than approximately 100 TDC counts) and smoothly rising for larger drift times up to a value which proved to scale linearly with the temperature differences as 25 μm/°C. In Fig.18 the $r-t$ difference as measured in different pairs of runs is shown. These variations, $\delta r(t)$, can be parametrized

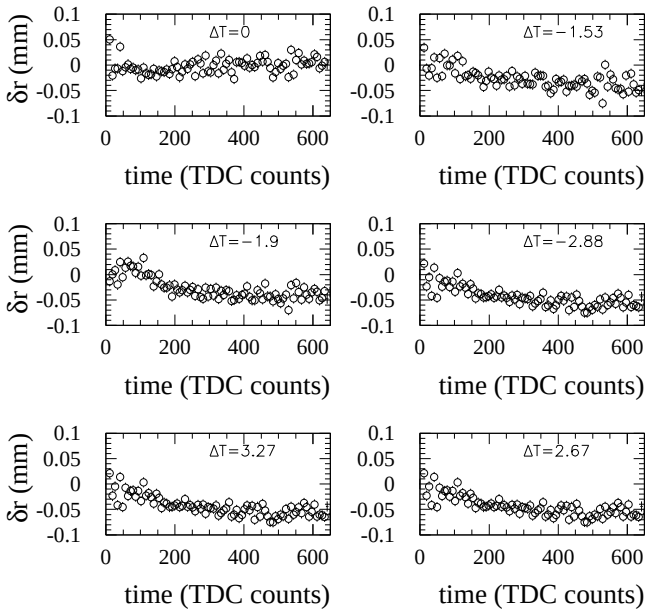

Fig. 18. Temperature effects as obtained from $BILrot$ data for different temperature variations (Summer data).

with the function:

$$\delta r(t) = \left(\frac{T + \Delta\, T}{T} - 1\right)\left[r(t) - t \cdot \frac{dr(t)}{dt}\right] \tag{3}$$

where T is the reference temperature (given in °K), ΔT is the temperature difference, and the time derivative of the $r-t$ function is computed with a fit with Chebytchev polynomials. To check this parametrization, the parameter ΔT has been determined with a fit to the $r-t$ differences and compared with the measured temperature changes. This correlation plot as obtained using runs with a 40 mV threshold, with the $BILrot$ in rotation by more than 6 degrees and with a number of events larger than 20k, is shown in Fig.19. The runs with a temperature lower than 22°C refer to the fall, the others to the summer period. The line shown in the figure is the bisector line. The good agreement between fitted and measured temperature values over a period of many months indicates the stability of the $r-t$ over time except for the well understood temperature effects.
The $r-t$ computed in the rotating BIL can be used also in the other chambers once corrected for temperature variation. This leads to good average residuals

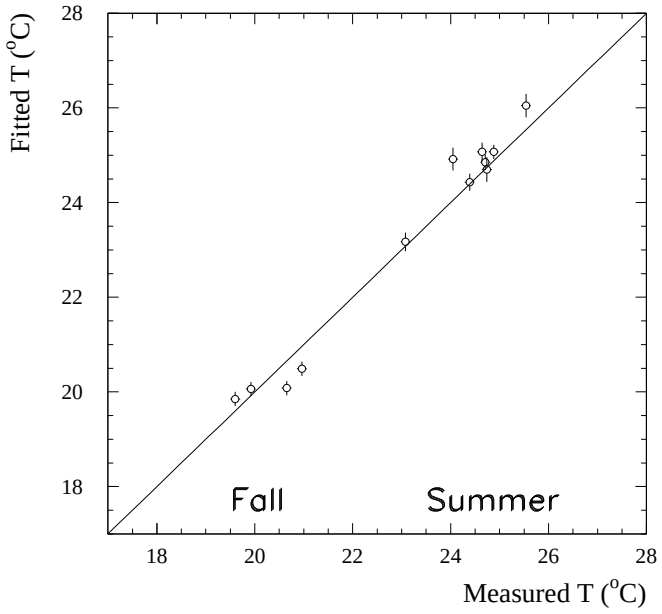

Fig. 19. Correlation plot between temperature as measured with probes and as derived from the variation of the $r-t$ relation in $BILrot$ data.

(of less than 20 μm) only if the gas properties of the chamber are close to those of the rotating BIL. This can be checked, for example, looking at the value of $t_{max}^{24^\circ}$ introduced in the previous section. Fig.20 shows the average residuals of barrel chambers as a function of drift time as obtained using a temperature corrected r(t) relation extrapolated from $BILrot$. The two parts of the figure refer to two different runs. Solid line histograms of each part refer to BIL and BML chambers while points refer to BOL chamber. In both runs the pattern is the same: while the residuals of inner chambers are within 20 μm at all times, BOL chambers show significantly larger average residuals. This may be correlated to the fact that the average t_{max} value of BOL is 4 TDC counts larger than the average of BIL and BML chambers. The t_{max} rms value of BIL and BML chambers of 0.70 TDC counts indicates that the difference is statistically significant. The observed change Δt_{max} in t_{max} is expected to induce residuals at a time t of the order $\approx \Delta t_{max}/t_{max} \times v_d(t)$ in good agreement with findings. This suggests a slightly different gas composition in the different chambers. In [15] the effect of the presence of Water, Nitrogen, Oxygen, Methane in the standard MDT gas mixture with has been studied. While Water is shown to induce a variation Δt_{max} in the t_{max} value like $\Delta t_{max} = .066\ ns\ /\ (ppm\ of\ Water)$, the other contaminants have a negligeable effect. The observed difference of the t_{max} value between BOL and BIL and BML chambers may then be attributed to the presence of ≈ 50 $(ppm\ of\ Water)$ due to the permeability of the plastic gas pipes, the tube O-rings and endplugs to Water.

7 Summary

The analysis of MDT calibration constants using the H8 2004 test beam data is presented in this paper. A large sample of runs taken during two periods in summer and fall and under different running conditions has been studied.
Existing simulation studies in ATLAS suggest that the target accuracies for the t_0 and $r-t$ MDT calibration constants are of 2 ns and 50 μm respectively. The determination of the parameters of the drift time spectra has been optimized using a Monte Carlo technique. This method provided an improved definition of the starting point of the drift time distribution, t_0, such that the resulting spread of the corresponding distribution is narrower than the 'classical' one. The same procedure has been used for the total drift time distribution, t_{max}, which also resulted in a narrower distribution than the 'classical' one.
A study of the data quality allowed the definition of selection criteria to be applied in the analysis. The study of test beam data has shown the drift time constants to be stable in time and the resulting spread of the distributions to be in good agreement with Monte Carlo predictions. In particular the t_0 trace plot of most populated tubes has been studied and found to be stable within

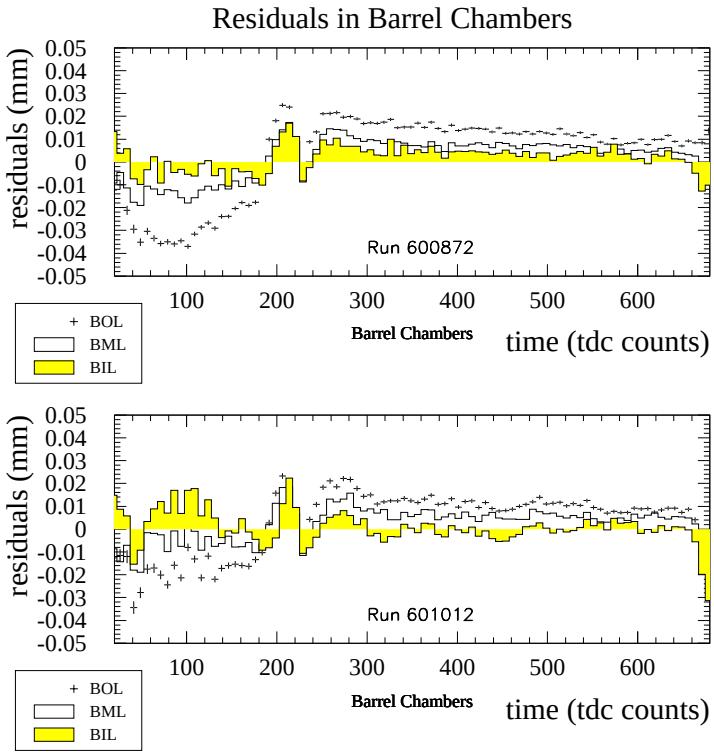

Fig. 20. Residuals versus drift time for barrel chambers in two different runs as obtained using a temperature corrected $r-t$ relation extrapolated from $BILrot$. While the residuals for BML and BIL are well inside $\pm 20 \mu m$, the deviations for the BOL are significantly larger.

0.5 TDC counts, corresponding to less than 0.4 ns, when using fall data. This result is valid for all chambers. The drift time stability was observed over a period of several months. The observed t_0 shift of 0.85 TDC counts between summer and fall data was interpreted as a temperature effect in agreement with the GARFIELD prediction.
The variation of t_0 with the discriminator threshold of MDT electronics has been studied and found to have a slope of about -0.13 ns/mV, in good agreement with the GARFIELD predictions.
The variation of the maximum drift time t_{max} with temperature is described by a linear dependence of t_{max} with respect to temperature with a slope of -2.5 ns/°C in agreement with previous measurements [14]. The comparison of the extrapolated t_{max} value at 27° C with the GARFIELD predictions at different gas compositions suggests that the effective gas composition at H8 was about $Ar\ CO_2$ of 93.5:6.5. The t_{max} of some chambers was observed to be larger than for all other chambers even after temperature correction. This might possibly be explained with a contamination of air, water vapor or a different pressure of the gas mixture, but no clear evidence has yet been found.
The $r-t$ relation has been studied using data from an MDT chamber mounted on a rotating support which allowed a proper angular spread for the calculation. Once corrected for temperature effects, the $r-t$ relation is found to be stable over the duration of the period of data taking.
In conclusion all MDT calibration constants have been found to be stable and calculable well below the required target accuracies.

Acknowledgments
We want to thank our friends of Roma Tre for many useful discussions on all the aspects of the analysis.
We also want to thank Alfredo Iaciofano for the construction and commissioning of the rotating support for the BILrot chamber.

A Study of MDT calibration constants using simulated data

A.1 t_0 study using simulated data

A Monte Carlo technique has been used to generate samples of drift time distributions originating from the same seed, being characterized by the same t_0. Samples of different sizes were be passed through the different fitting procedures and the corresponding spread of the distribution of reconstructed t_0's indicates the accuracy of the reconstruction method. The analysis of Monte Carlo simulated samples allows the comparison of the following t_0 reconstruction methods introduced in section 4:

(1) Classic t_0
(2) Fermi Dirac t_0: fit with a 3 parameter fit + constant value;
(3) Displaced Classic t_0: optimized Classic t_0
(4) Displaced Fermi Dirac t_0: Fermi Dirac t_0

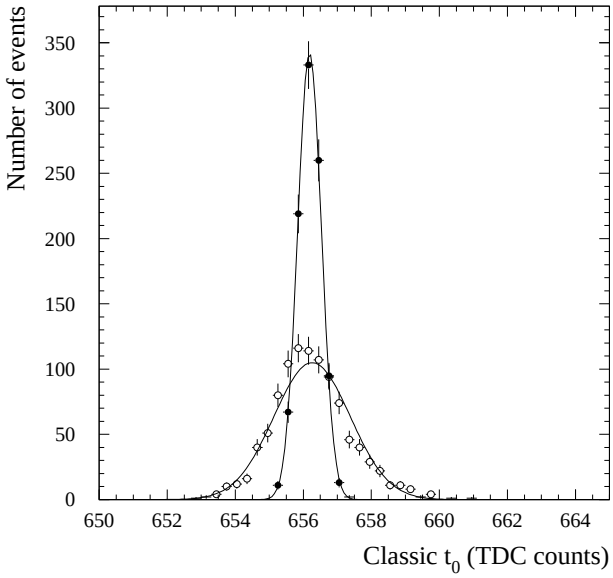

Fig. A.1. t_0 Classic distribution as obtained with a sample of 5k events and 50k events, black dots and open circles distribution respectively

The drift time distribution of a single tube obtained with a sample of 1.2M test beam muons, taken at the same discriminator threshold and in a limited period of time which ensured that the gas conditions remained constant, has been used as a reference for generating drift time distributions. Thousand independent runs with 2,5,10,20,50 k-events were generated. The drift time distribution of each simulated run was then passed through the t_0 reconstruction algorithms described in section 4. The resulting distributions of the t_0's in different runs were fitted with a Gaussian distribution and the average values and the widths were recorded. Fig. A.1 shows the distribution of t_0 Classic in 1000 runs with 50 and 5 kevents respectively, the former being, as expected, much narrower. The fitted Gaussian distributions of the two samples are also shown.

The width of the t_0 Classic distribution as a function of the sample size is shown if Fig. A.2 for data (open triangles) and GARFIELD simulation (open circles). The agreement between data and simulation is good.

The top part of Fig. A.3 shows the distribution of leading edge slope and the Classic t_0 as observed in the run with 50K entries. The bottom part of this figure shows the correlation plot of these two quantities. They are clearly positively correlated. This observation suggests that the parameter which is

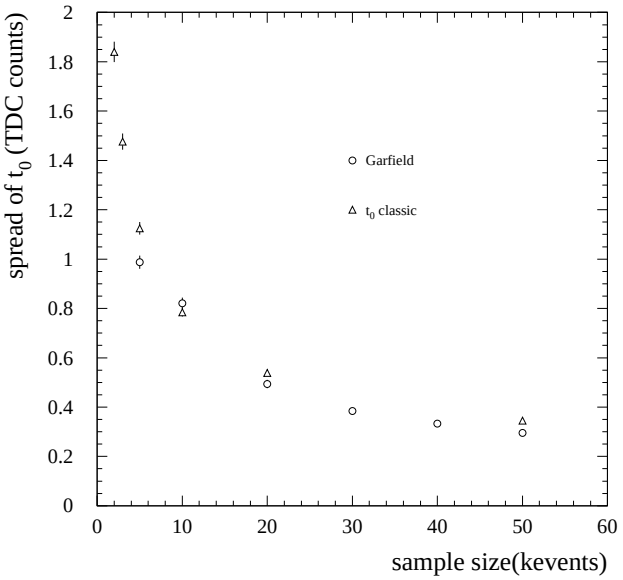

Fig. A.2. Spread of t_0 distribution as a function of the sample size for the t_0 Classic method (triangles) and GARFIELD (open circles)

used to characterize the start of the MDT drift distribution and to equalize different tubes may be optimized, to minimize the spread of the distribution, by correcting the initial value of Classic t_0 by a number of times the fitted slope. This may be investigated by studying how the spread of the Classic t_0 around its average value changes when replacing Classic t_0 with

$$\text{Displaced Classic } t_0 = \text{Classic } t_0 \text{ - } \textit{correction factor} \times \textit{slope}$$

The result of this analysis is shown in Fig A.4. The top part of the figure shows the average width of Displaced Classic t_0 as a function of the $correctionfactor$ and for different statistical samples. The minimum spread is obtained with a choice of the $correctionfactor$ equal to 1.5 for all statistical samples. The bottom part of Fig. A.4 shows the average Displaced Classic t_0 as a function of the $correctionfactor$. The dependence is obviously linear and a $correctionfactor$ equal to 1.5 induces a reduction of about 6 TDC counts with respect to Classic t_0, corresponding to $correctionfactor$ equal to 0. The Displaced Fermi Dirac t_0 is defined in a way similar to Displaced Classic t_0 as

$$\text{Displaced Fermi Dirac } t_0 = \text{Fermi Dirac } t_0 \text{ - } \textit{correction factor} \times \textit{slope}$$

Fig. A.5 shows the average value of the t_0 distribution as reconstructed by the four different algorithms indicated above and as a function of the sample size: open circles correspond to Classic t_0, open diamonds to Fermi Dirac t_0, open triangles to Displaced Classic t_0 and thick crosses to Displaced Fermi Dirac t_0. The four algorithms give different average values thus corresponding to

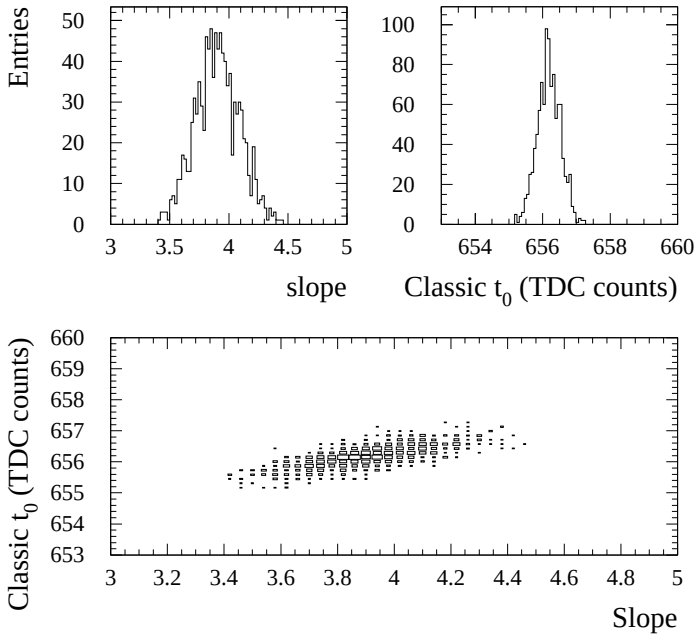

Fig. A.3. Top part: distribution of leading edge slope and of the Classic t_0; Bottom part: correlation plot of the two above quantitites.

different position of the raising edge. The Classic t_0 gives the highest t_0 value, the Displaced Fermi Dirac t_0 gives the lowest t_0 value, the Fermi Dirac t_0 is between the two. The Displaced Classic t_0 is very close to the Displaced Fermi Dirac t_0. All four methods give average t_0's which are nearly independent of the sample size.
The corresponding width of the t_0 distribution as a function of the sample size is shown if Fig. A.6. The width of the t_0 distribution is observed to scale approximately as a $1/\sqrt{N}$ as expected, where N is the sample size. Furthermore the Displaced Classic t_0 algorithm is systematically better than the three other algorithms and gives a width of 0.75 TDC counts for samples of 5k events and 0.25 TDC counts for samples of 50k events. The Classic t_0 is the worst method while the Displaced Fermi Dirac is the second best, therefore the Displaced Classic t_0 will be used to get all results shown in the following.

A.2 t_{max} study using simulated data

A procedure similar to that used to find the best t_0 indicator has been used to study the measurement of the drift spectrum width. The Fermi Dirac function which describes the trailing edge of the drift spectrum is characterized by a t_1

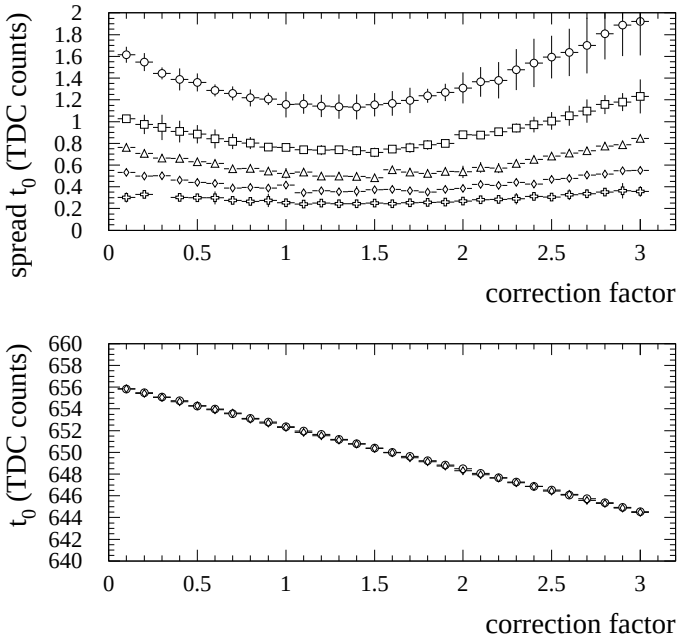

Fig. A.4. Top part: width of Displaced t_0 Classic distribution for different statistical samples. Families of points from top to bottom correspond to samples of 2,5,10,20,50 k events; Bottom part: average of Displaced t_0 Classic distribution for different statistical samples

value and by a trailing edge slope $slope_{te}$. However, the important quantity is not t_1 but the drift spectrum length t_{max}, defined to be $t_1 - t_0$. Similarly to the corrected definition of t_0, the quantity

$$\text{Displaced } t_{max} = t_1 + \textit{correction factor} \times slope_{te} \text{ - } \textit{Displaced Classic } t_0$$

has been studied to find the value of the $correction factor$ which gives the minimum spread of t_{max}. Fig. A.7 shows the result of this analysis. The spread of the Displaced t_{max} distribution as a function of the correction factor and for different statistical samples is shown in the top part of the figure while the average value of the Displaced t_{max} distribution as a function of the correction factor and for different statistical samples is shown in the bottom part. As in the case of t_0 also for the case of t_{max} the minimum is reached for a value of the $correction factor$ which is equal to about 1.2. The net variation of the new definition of t_{max} which corresponds to the best measuring situation corresponds to an increase of about 20 TDC counts with respect to the standard 8 parameters fit function. A spread of 2.9 and 1.0 TDC counts is observed for sample sizes of 5000 and 50000 events respectively.

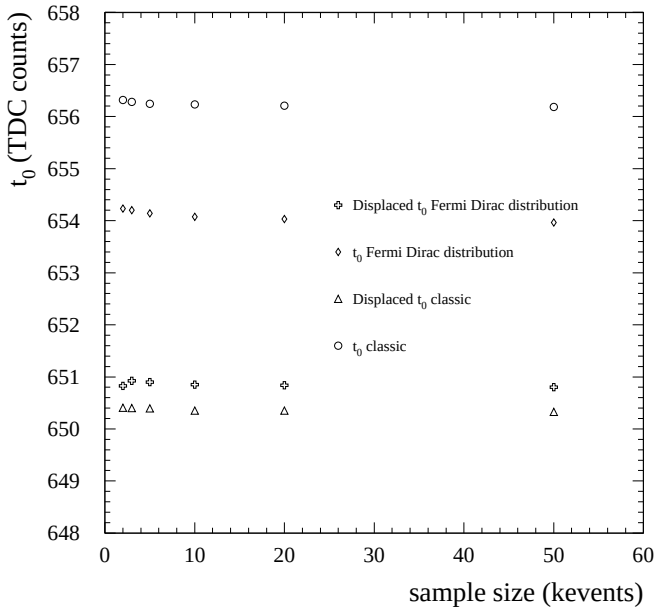

Fig. A.5. Average t_0 as a function of the sample size for the t_0 Classic method (open circles), Displaced t_0 (open triangles), FermiDirac (open diamond), Displaced Fermi Dirac t_0 (thick crosses).

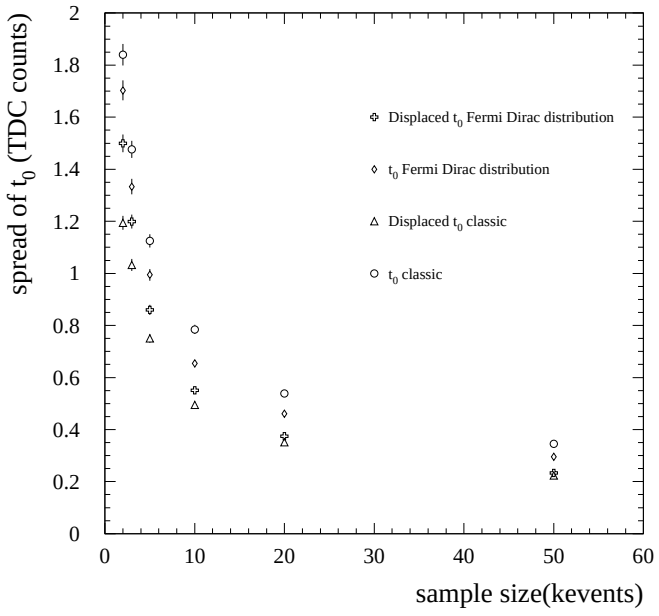

Fig. A.6. Spread of t_0 distribution as a function of the sample size for the t_0 Classic method (open circles), Displaced t_0 (open triangles), FermiDirac (open diamond), Displaced Fermi Dirac t_0 (thick crosses).

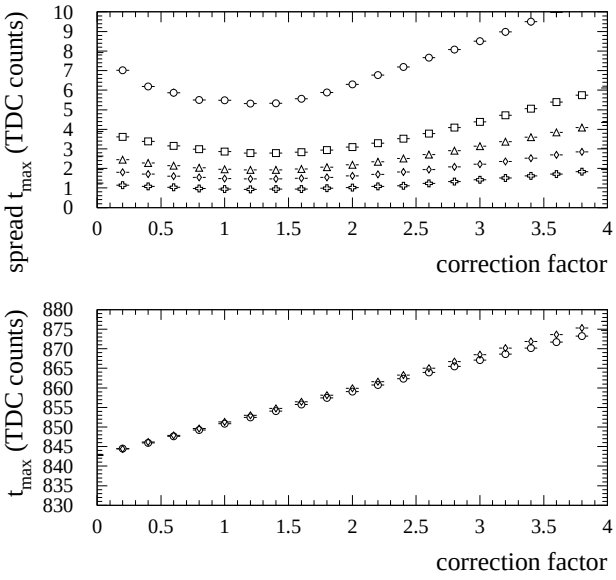

Fig. A.7. Top part: spread of Displaced t_{max} distribution as a function of the correction factor and for different statistical samples. Families of points from top to bottom correspond to samples of 2,5,10,20,50 k events; Bottom part: average of Displaced t_{max} distribution as a function of the correction factor and for different statistical samples

Possible beam profile induced systematics have also been studied using the same Monte Carlo technique as used to study t_0 reconstruction. The drift time distribution as measured in one MDT tube reflects the radial distribution of the tracks in this tube. In contrast to the situation in ATLAS the MDT chambers are not illuminated in a homogeneous way, the H8 beam being very narrow: most of the beam muons are contained in a few centimeters. This induces an uneven radial distribution of tracks in the different MDT tubes which depends on the location of the tube in the beam profile. To study this effect, the seed drift distribution has been folded with the measured beam profile. Different simulation points, corresponding to different positions of the tube have been considered. Each drift time has been weighted according to the radial distribution in that tube using the radius computed from the inverse of the $r - t$ function. The beam biased drift time distribution was then passed through the same t_0 reconstruction program as described above. Each generated sample contains the same number of events. The result of this analysis is shown in Fig. A.8. The top part of the figure shows the profile of the H8 beam as measured by the BOL MDT chamber while the bottom part shows the average reconstructed t_0 as a function of the tube position in the beam

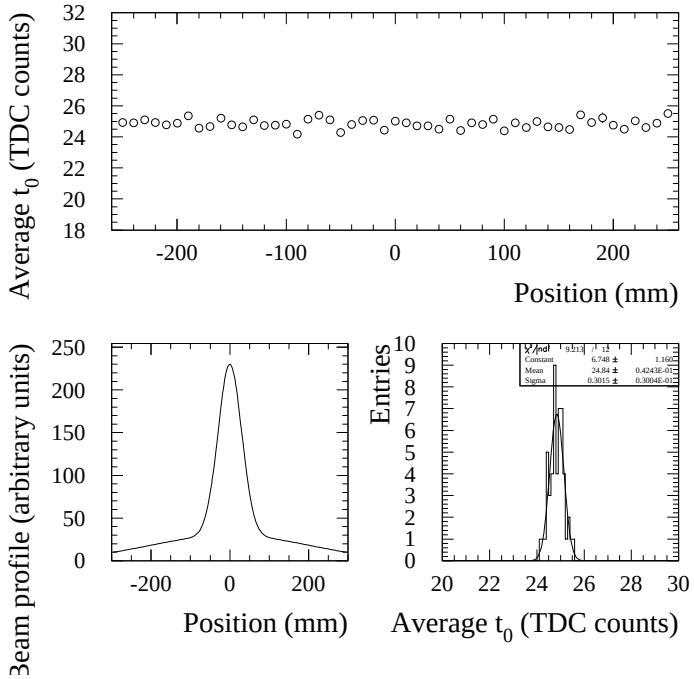

Fig. A.8. Top part: profile of the H8 beam as measured by the BOL MDT chamber; bottom part average reconstructed t_0 as a function of the tube position in the beam profile

profile. All reconstructed t_0's are within $\pm$ 1 TDC count. Thus no significant, systematics is induced by the beam profile which was found not to modify the shape of the resulting drift time distribution in one tube.

B The simulation with GARFIELD

In this section a brief description of the main settings chosen to configure the program is reported. The calculation time of the MAGBOLTZ program is not negligble, therefore the two most critical values in this respect, namely `n-e` and `coll`, must be initialized according to the specific needs as described in what follows. MAGBOLTZ will compute the transport properties for discrete electric field values that are regularly distributed within a given range. The values reported in table B.1 corresponds to the electric field at the MDT anode and cathode surface. On one hand the number of points must be large enough so as to represent any fine structure that may be present in the transport properties. On the other hand, an excessively large number of points may lead to oscillations in the interpolation and to a larger computing time (which increases linearly with this parameter). Previous estimations suggest 40 logaritmically spaced points (adjusted through the `n-e` parameter, cfr. tab. B.1) as the optimal choice for the kind of simulation presented here (i.e. arrival time distributions, $r-t$ relation, etc). The parameter `coll` specifies the number of collisions, in multiplies of 960000, to be used to compute the transport properties at each electric field point. It is worth noticing that the CPU time consumption increases linearly with this parameter while the statistical accuracy of the drift parameters calculation improves with its square root. The chosen value of 20 leads to a statistical error of 0.2% on the drift velocity, 2% on the transverse diffusion and 3.5% on the longitudinal diffusion. MAGBOLTZ only computes the electron transport properties, not the ion ones. The ion mobility can be fixed to a constant value or, if the depence on the electric field is not negligible, can be provided in tabular form as a function of the reduced electric field. The mobility of the gas mixture has been approximated to the mobility of pure Argon (Ar^+/Ar). The values provided, as reported in [16], are shown in the scatter plot of Fig. B.1.left. The gas temperature and composition are adjusted as needed. The GARFIELD program simulates the drift of the ionization electrons by taking into account both the diffusion and the attachment in the gas. The effect of delta electrons has been simulated as well. A Polya distribution with parameter $\theta = 0.38$ was used to describe the statistical fluctuation of the gas amplification (`gain`) around the mean value which has been fixed to 2×10^4. The signal propagation along the anode wire and the properties of the front end electronics (ASD) were taken into account by folding the raw current signal $I(t)$ (Fig. B.2.left) with the transfer functions of an MDT and the ASD amplifier-shaper circuit. The transfer function of a

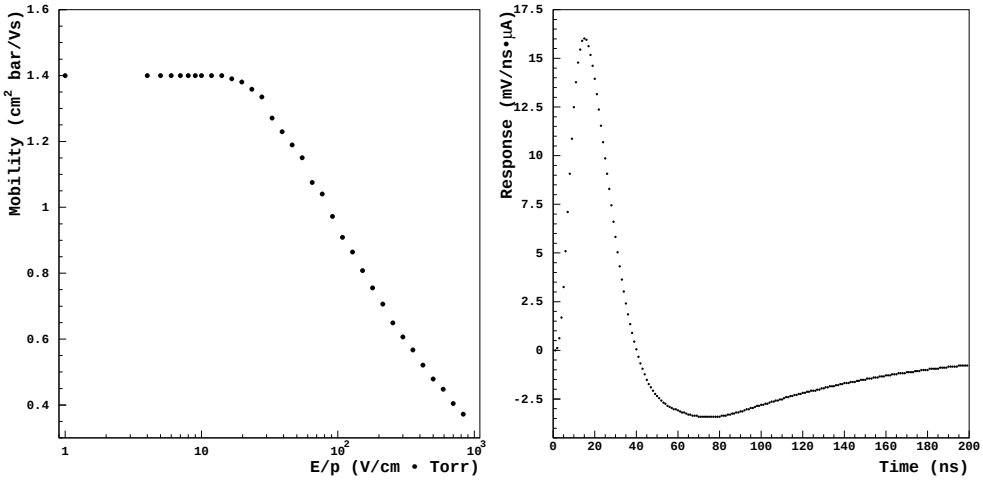

Fig. B.1. *Left*: mobility of Ar^+ in Ar with respect to the reduced electric field. *Right*: transfer function for bipolar shaping with 15 ns peaking time.

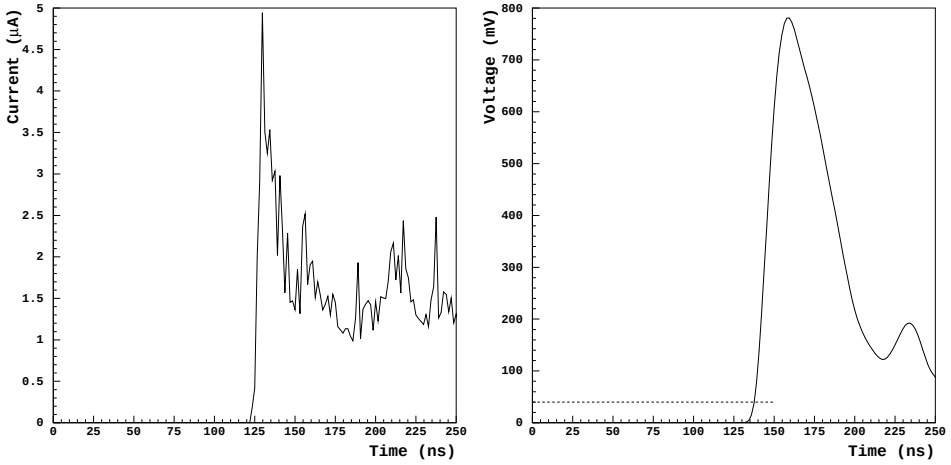

Fig. B.2. *Left*: a typical current signal induced by a muon travesing the tube at a distance of 0.5 cm to the wire. *Right*: the same signal after the convolution with the transfer function of Fig. B.1. The dashed line corresponds to a 40 mV threshold.

bipolar shaper circuit with 15 ns peaking time has been provided in tabular form. The values are shown in Fig. B.1.right. Signals have been computed in the time range from 0 to 0.78125 μs and sampled every 0.78125 ns (adjusted trough the `window` and `step` parameters, cfr. tab. B.1) which corresponds to the AMT TDC chip resolution. The output of the current signal convolution is a voltage signal $V(t)$ (Fig. B.2.right) as seen by the discriminator. The TDC time associated to the passage of a ionizing particle is defined as the time at which the signal $V(t)$ crosses a given threshold, in multiplies of 0.78125 ns. The TDC time distributions used in the present analysis have been produced by generating samples of 170 GeV muons at random distances from the anode wire. All the reported settings are summarized in tab. B.1.

MAGBOLTZ	
Parameter	*Value*
`coll`	20
`e/p-range` $(V/cm \cdot Torr)$	0.14718 - 85.9527
`n-e`	40
GARFIELD	
Parameter	*Value/Status*
`gain`	2×10^4
`polya`	0.38
`diffusion`	on
`attachment`	on
`delta-electron`	on
`window` (μs)	0 - 0.78125
`step` (μs)	0.00078125

Table B.1
Main parameter settings specified for the MAGBOLTZ and GARFIELD initialization.

References

[1] The ATLAS Muon Spectrometer Technical Design Report, CERN-LHCC/97-22 (1997);
S.Palestini, Nuclear Physics B (Proc.Suppl.) 125 (2003) 337

[2] Tile Calorimeter Technical Design Report, CERN-LHCC/96-42 (1996);

[3] Liquid Argon Calorimeter, Technical Design Report, CERN-LHCC/96-41 (1996);

[4] J.E.Huth, J.Oliver, E.S.Hazen, C.Posch, J.T.Shank, Development of an octal CMOS ASD for the ATLAS Muon detector, Proceedings of the 5th Conference on Electronics for LHC Experiments, Snowmass, CO, 20-24 September 1999, p.436;
C.Posch, E.Hazen, and J.Oliver, MDT-ASD: CMOS front-end for ATLAS MDT chambers, ATL-MUON-2002-003; 7.6.2001,
`http://weblib.cern.ch/Home/ATLAS_Collection/ATLAS_Notes/Muon/`

[5] Y.Arai, Nucl. Instr. and Meth. in Phys. Res. A453 (2000) 365;
Y.Arai, Y.Kurumisawa and T.Emura, Development and a SEU Test of a TDC LSI for the ATLAS Muon Detector, Proceedings of the 7th Workshop on Electronics for LHC Experiments, Stockholm, Sweden, 10-14 September 2001, p.185.

[6] J.Chapman et al., Data flow simulations through the ATLAS Muon front-end electronics, Proceedings of the 5th Conference on Electronics for LHC Experiments, Snowmass, CO, 20-24 September 1999, p.448.

[7] M.Boterenbrood et al., Design and implementation of the ATLAS detector control system, IEEE Trans. Nucl. Sci., 51 (2004) 495-501.
M.Boterenbrood, B.Hallgren, The development of Embedded Local Monitor (ELMB), Proceedings of the 9th Workshop on electronics for the LHC Experiments, LECC 2003, Amsterdam, The Netherlands, 29 Sep - 3 Oct 2003, p.331-334.

[8] G.Avolio et al., Nucl. Instr. and Meth. in Phys. Res. A523 (2004) 309.

[9] P.Bagnaia et al., CALIB: a Package for MDT Calibration Studies, ATL-MUON-2005-013 (2002),
`http://weblib.cern.ch/Home/ATLAS_Collection/ATLAS_Notes/Muon/`

[10] Igor Smirnov, *HEED, program to compute energy loss of particles in gases*, Version 1.01, CERN Program Library.

[11] S. Biagi, *MAGBOLTZ, program to compute gas transport parameters*, Version 1.10, CERN Program Library.

[12] R.Veenhof, *GARFIELD - Simulation of gazeous detectors*, Cern Program Library W5050.

[13] N.van Eldik, The ATLAS muon spectrometer: calibration and pattern recognition. Thesis, ISBN-10:90-6464-071-8

[14] A.Branchini et al, Study of drift properties of high pressure drift tubes for the ATLAS muon spectrometer, IEEE Trans. Nucl. Sci. 53-1 (2006) 317-321. F.Cerutti et al., Study of the MDT drift properties under different gas conditions, ATLAS-MUON-PUB-2006-004 (2003), `http://weblib.cern.ch/Home/ATLAS_Collection/ATLAS_Notes/Muon/`

[15] R.M.Avramidou, R.Veenhof, Dependence of the MDT chambers drift time on the gas mixture, ATL-COM-MUON-2005-011 (2004), `http://weblib.cern.ch/Home/ATLAS_Collection/ATLAS_Notes/Muon/`

[16] W.Blum, L.Rolandi, *Particle Detection with Drift Chambers*, Springer-Verlag (1993).